Population balances combined with computational fluid dynamics : a modeling approach for dispersive mixing in a high pressure homogenizer

Chemical Engineering Science 117 (2014) 376–388

Contents lists available at ScienceDirect

Chemical Engineering Science

journal homepage: www.elsevier.com/locate/ces

Population balances combined with Computational Fluid Dynamics: A modeling approach for dispersive mixing in a high pressure homogenizer

Arend Dubbelboer [a], Jo Janssen [b], Hans Hoogland [b], Ashvin Mudaliar [b], Shashank Maindarkar [c], Edwin Zondervan [a], Jan Meuldijk [a,*]

[a] Department of Chemical Engineering and Chemistry, Technical University of Eindhoven, PO Box 513, 5600 MB Eindhoven, The Netherlands
[b] Structured Materials & Process Science, Unilever Research, Olivier van Noortlaan 120, 1330 AC Vlaardingen, The Netherlands
[c] Department of Chemical Engineering, University of Massachusetts, Amherst, MA 01003-9303, United States

HIGHLIGHTS

- The pressure drop and the number of passes were examined in a homogenizer.
- Population balances combined with CFD were used to model the droplet sizes.
- Four compartments were defined around the high speed jet.
- One set of parameters was found covering all hydrodynamic conditions.
- The model predictions have improved by 65% compared to a single compartment model.

ARTICLE INFO

Article history:
Received 7 April 2014
Received in revised form
26 June 2014
Accepted 30 June 2014
Available online 8 July 2014

Keywords:
Emulsification
High pressure homogenizer
Population balance equations
Computational Fluid Dynamics
Turbulence

ABSTRACT

High pressure homogenization is at the heart of many emulsification processes in the food, personal care and pharmaceutical industry. The droplet size distribution is an important property for product quality and is aimed to be controlled in the process. Therefore a population balance model was built in order to predict the droplet size distribution subject to various hydrodynamic conditions found in a high pressure homogenizer. The hydrodynamics were simulated using Computational Fluid Dynamics and the turbulence was modeled with a RANS k–ε model. The high energy zone in the high pressure homogenizer was divided into four compartments. The compartments had to be small enough to secure nearly homogeneous turbulent dissipation rates but large enough to hold a population of droplets. A population balance equation describing breakage and coalescence of oil droplets in turbulent flow was solved for every compartment. One set of parameters was found which could describe the development of the droplet size distribution in the high pressure homogenizer with varying pressure drop. An improvement of 65% was found compared to the same model containing just one compartment. The compartment approach may provide an alternative to direct coupling of CFD and population balances.

1. Introduction

Many emulsified consumer products contain micron or even submicron sized droplets, for example mayonnaise, cream liquors, margarine and lotions. The droplet size is important for many product properties like appearance, stability (McClements and Chanamai, 2002), rheology (Luckham and Michael, 1999; Scheffold et al., 2013) and controlled release of substances (McClements and Yan, 2010). It is therefore of interest to control the droplet size during the production process. A typical production process consists of two steps: in the first step oil and water phases are mixed, possibly with other ingredients, forming a coarse emulsion; then, in the second step the droplet size of the dispersed phase is further reduced to a desired value. High pressure homogenization valves are often applied in the second step where they are able to generate submicron droplet sizes (Karbstein and Schubert, 1995; Schultz et al., 2004). A high pressure homogenizer consists of a pump and a homogenizing nozzle (Schuchmann and Schubert, 2001). The coarse emulsion is entering from the bottom along the main axis. The emulsion hits a solid impact head and spreads out through the narrow gap in the radial direction (Fig. 1). This type of homogenizing valve is

* Corresponding author. Tel.: +31 40 247 2328.
E-mail address: j.meuldijk@tue.nl (J. Meuldijk).

http://dx.doi.org/10.1016/j.ces.2014.06.047
0009-2509/

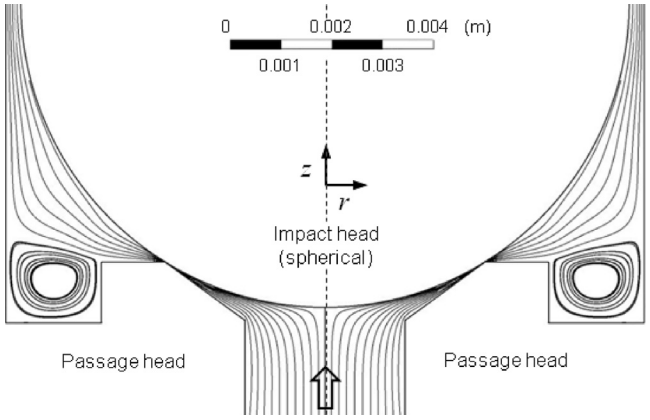

Fig. 1. The geometry of the high pressure homogenzier.

commonly referred to as a radial diffuser (Phipps, 1975; Schultz et al., 2004).

Although high pressure homogenizers are already utilized in industry for over a century, they remain a topic for scientific study. In the last decade, many researchers have tried to simulate the emulsification process inside the homogenizer valve, each using a different approach. For example, population balance equations (PBE) were developed to track the change of the droplet size distribution inside a homogenizer (Håkansson et al., 2009; Maindarkar et al., 2012; Raikar et al., 2009, 2010, 2011). The PBE models described the breakage and coalescence of droplets and the adsorption of emulsifier molecules (Håkansson et al., 2013b; Maindarkar et al., 2013). The advantage of using this approach is that the complete droplet size distribution could be retained. One drawback is that often 4–6 parameters are necessary to obtain a proper fit of the experimental data. These approaches are mainly based on the average energy dissipation over the valve. This means that no homogenizer geometry characteristics could be included and the fit parameters are equipment dependent and even pressure dependent for the same equipment (Maindarkar et al., 2012; Raikar et al., 2011). To allow predictions of the droplet size distribution it is necessary to have a single set of parameters describing the change in the droplet size distribution experiencing different pressures for one type of equipment and even for various geometries this would be desirable.

Improvements can be made when more hydrodynamic features are incorporated. This could be achieved with tools like Computational Fluid Dynamics (CFD), where locally, inside the apparatus, shear rates and turbulent energy dissipation rates can be calculated. Many studies have focused on the flow patterns inside high pressure homogenizers, and predicted average stable droplet sizes from CFD-simulations (Casoli et al., 2010; Floury et al., 2004a, 2004b; Steiner et al., 2006). Some laboratories compared the CFD simulations with Particle Image Velocimetry (PIV) measurements (Blonski et al., 2007; Håkansson et al., 2013a; Innings and Trägårdh, 2007). It remains practically impossible to measure the velocity field inside real homogenizers because of the tiny geometry and high velocities. Therefore scaled model homogenizers were fabricated (Blonski et al., 2007; Innings and Trägårdh, 2007). The main conclusions from comparing simulations to measurements of the scaled homogenizer were that the Reynolds Averaged Navier Stokes (RANS) k–ε models are able to describe the flow in the turbulent region qualitatively (Håkansson et al., 2012).

Solving PBEs and CFD simulations take up a lot of computing power. Integration of the two techniques requires even more computing power. Advancing towards more detailed modeling of emulsification processes has resulted in a number of publications focusing on the coupling between the two techniques (Agterof et al., 2003; Becker et al., 2013; Drumm et al., 2009; Fathi Roudsari et al., 2012). To limit the calculation times, the moments of the particle size distribution were linked to CFD simulations for droplet size predictions (Agterof et al., 2003). The Direct Quadrature Method of Moments (DQMOM) solution of the population balance equation was implemented in CFD codes without increasing the computational costs too much (Drumm et al., 2009; Silva et al., 2008). Current versions of Fluent ANSYS are now equipped with DQMOM and QMOM and up to eight moments of the particle size distribution can be calculated. Algorithms have been developed to reconstruct any particle size distribution based on a finite number of moments (de Souza et al., 2010; John et al., 2007). Using these advanced algorithms in combination with CFD-QMOM could allow us to model the droplet size distribution for different hydrodynamic conditions. The accuracy of such an approach is yet to be investigated and the computational effort is expected to be high. Also, fully discretized PBEs coupled to CFD have been reported for emulsification systems (Becker et al., 2013; Fathi Roudsari et al., 2012). Fathi Roudsari et al. (2012) have been looking at the cumulative droplet size distribution for different hydrodynamic conditions in a stirred tank, i.e. the impeller speed was varied. Becker et al. (2013) have looked into a coupled PBE-CFD modeling framework for a high pressure homogenizer which runs only at a constant pressure drop. For systems where the geometry is confined to a space comparable to the droplet size it is physically not realistic to solve a balance for the whole population of droplets. Then one has to define compartments which are physically large enough to contain a population of droplets but small enough to ensure a low variation in the turbulent energy dissipation. This approach has been used in the past for stirred tanks, where the tank has been divided up into two (Alexopoulos et al., 2002; Almeida-Rivera and Bongers, 2010) or 11 (Alopaeus et al., 1999) zones based on the distribution of energy dissipation rates. The compartment approach has not yet been encountered in the literature for emulsification in high pressure homogenization valves under varying hydrodynamic conditions.

The aim of the work described in this paper was to construct a compartment model of a high pressure homogenizer, which enables predictions of droplet size distributions without the need to fit all the experiments separately. The experiments were performed with varying hydrodynamic conditions. The hydrodynamic conditions in the valve changed when the pressure drop was varied. To be predictive, the model should work outside the experimentally verified ranges. Therefore one set of parameters is needed to describe the evolution of the droplet size distribution over the whole pressure range of the apparatus. To accomplish this, a population balance model was built describing breakage and coalescence of oil droplets in an aqueous dispersion. A lot of models have been suggested in the past to describe the breakage and coalescence of droplets and bubbles; see for example the review papers of Liao and Lucas (2009, 2010). There are models available which do not include experimentally tunable parameters. The breakage rate model from Luo and Svendsen (1996) has been tested for a radial diffuser type homogenizer, these results were not satisfying (see Becker et al., 2013). Instead the breakage and coalescence functions from Coulaloglou and Tavlarides (1977) were used. They form the backbone of most breakage and coalescence models for turbulent flow (Liao and Lucas, 2009, 2010). The free parameters in the breakage and coalescence functions were optimized so that the modeled size distributions matched the experimentally obtained droplet size distributions. The experiments were carried out by changing the pressure drop for a single emulsion formulation. Four different compartments were defined inside the device to account for the large turbulent inhomogeneities. The compartments sizes were based on the jet length. The jet length was approximated with an algebraic model based on a free shear flow assumption, see Section 3. The average energy dissipation rates in the compartments were

estimated with a k–ε turbulent model. Then the energy dissipation rates were fed to the breakage and coalescence kernels of the population balance model. The performance of a four compartment model was compared to that of a single compartment model and a two compartment model.

2. Experimental methods

To generate a pre-emulsion for homogenization, 1 wt% of Pluronic F68 emulsifying agent (Sigma Aldrich) was dissolved in Nanopure demineralized water. Subsequently 10 wt% of sunflower oil was slowly added while stirring with a Silverson L5T mixer. The Silverson mixer was equipped with a General Purpose Disintegrating Head and a Standard Emulsor Screen. The mixture was stirred for 5 min at 6000 rpm, the resulting d32 and dv99 were 15 and 54 μm, respectively. The droplet size distributions of all samples were measured with a static light scattering device (Malvern Mastersizer 2000). The viscosities of the sunflower oil and the Pluronic F68 solution were 50 and 1.3 mPa s, respectively. They were measured with a rotational shear rheometer (2000EX, TA Instruments) at a constant temperature of 25 °C. The equilibrium surface tension was carefully determined by Maindarkar et al. (2013) for a vegetable oil in water emulsion stabilized by Pluronic F68. At 25 °C and with a Pluronic concentration of 1.3 mol/m^3 the surface tension is 17 mN/m.

For homogenization a lab scale Niro Soavi high pressure homogenizer was used (type: Panda NS1001L). It was operated with a reciprocating multi-plunger pump. The homogenizer had a constant throughput of 13 l/h. A manual valve controlled the pressure drop. The pressure was varied between 200 and 800 bar. The pressure remained constant within +20 and −20 bar of the target pressure. The coarse emulsion was passed several times through the high pressure homogenizer. The reproducibility of the experiments was checked by repeating the homogenization experiments at 200 and 800 bar (Fig. 2a and b). The differences in the measured droplet size distributions were quantified using an objective function (Ψ), see Eq. (28) and also Maindarkar et al. (2012) and Raikar et al. (2009). In the optimization of the free parameters the modeled droplet size distributions are therefore converged when $\Psi \leq 0.006$. All experiments were performed with the same coarse emulsion.

3. Compartment sizing

In a previous contribution it was already shown that for this type of homogenizer breakup is likely to happen in the jet leaving the narrow restriction (Dubbelboer et al., 2013). This was found for other similar types of homogenizers as well (Innings and Trägårdh, 2007). Therefore the compartments need to be defined in the jet area. The height of the compartments is restricted by the valve impact and passage heads. Only the length of the compartments in the radial direction must be estimated and this is based on the jet length. The jet is spreading in a radial direction and is expected to die out sooner than, for example, a planar jet for which algebraic equations are readily available in most textbooks. Algebraic equations for the planar and round jets are surprisingly accurate when compared to experiments. The flows in planar and round jets are the so-called free shear flows, where there is no influence of solid boundaries above or below the jet. Then it appears that the momentum in the jet is conserved and the spreading rate is constant. In fact, the spreading angle of the jet for both geometries was found to be around 12°. When the jet was assumed to be of the free-shear-flow type the radial spreading of the jet can be described by

$$\frac{\bar{u}_0}{U_0} = \left(1 + \frac{\alpha}{2}\left(\frac{r^2 - r_0^2}{r_0 \delta_0}\right)\right)^{-1/2} \quad (1)$$

In which $\bar{u}_0$ is the average center line jet speed, U_0 is the center line jet speed at r_0, δ_0 is the jet width at r_0, α is the entrainment coefficient and r_0 is the point where the jet becomes self-similar. Because planar and round jets both have an entrainment coefficient of 0.42 the same entrainment coefficient was assumed for the radial jet. The distance the jet spreads in the radial direction can now be estimated with Eq. (1). The starting jet width is taken equal to the spatial distance between the passage and impact

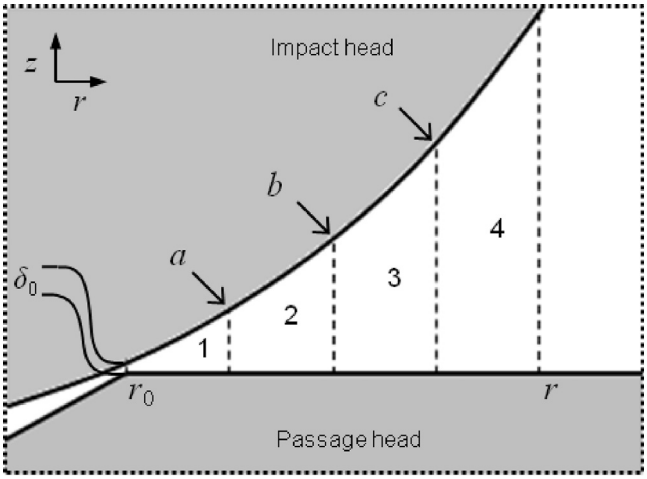

Fig. 3. The region between the impact and passage head directly after the gap with the 4 compartments, the boundaries between the compartments are designated as *a*, *b* and *c*.

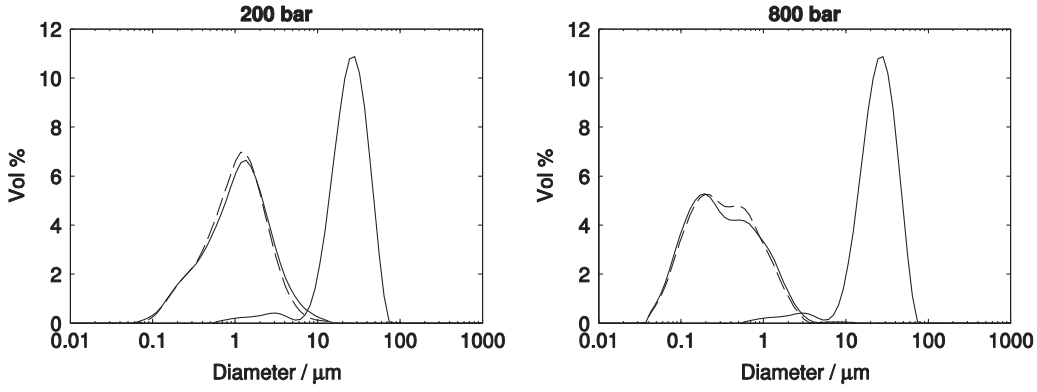

Fig. 2. The inlet (gray line), outlet (black line) and repeated outlet (black dashed line) droplet size distributions measured with a static light scattering device; left, after 1 pass at 200 bar with Ψ=0.0057 and right, after 1 pass at 800 bar with Ψ=0.0060.

Table 1
The compartment volumes and mean residence times.

Compartment	V/m^3	t_{res}/s
1	8.9E−12	2.4E−06
2	2.6E−11	7.1E−06
3	4.4E−11	1.2E−05
4	6.3E−11	1.7E−05

head. These gap heights were estimated by Dubbelboer et al. (2013). For a decay of 90%, with r_0 is 2.5 mm and δ_0 is 0.0016 mm, the jet reaches to 2.9 mm in the radial direction. The single compartment model has a compartment which reaches from r_0 to r. A two compartment model was made which contained two compartments divided equally over the distance r–r_0. Likewise the four compartment model has four compartments divided equally over the distance r–r_0, see Fig. 3. The resulting compartment volumes and residence times of the four compartments are given in Table 1. The residence time in a compartment should be sufficient for droplet breakup to occur. This will be checked by analyzing the time scales for turbulence and droplet deformation in Section 5.

The compartments are placed in series where the outlet of compartment one was the inlet for compartment two and so forth. A population balance was solved for every compartment. The first requirement for the application of the PBE method is that the control volume must be large enough to contain a population of particles. There are no clear criteria available, but here the number of particles in compartment one becomes $\phi V_1/(\pi d_{32}^3/6)\sim 10^6$, which is believed to be sufficiently large for the use of population balance methods in this tiny geometry. Now that the compartments are defined the hydrodynamic forces inside the compartments must be determined. The hydrodynamic pressure for example is responsible for droplet fragmentation and is related to the energy dissipation. The turbulent energy dissipation in each compartment was estimated using the infamous k–ε model.

4. Computational Fluid Dynamics

High velocity jets have turbulent characteristics; therefore a turbulence modeling approach has to be adopted. The first assumption made was the single phase approximation. It was assumed that the dispersed oil droplets move with the same speed as the continuous phase. Therefore the emulsion was modeled as a quasi single phase with an average density and an average Newtonian viscosity. Then, the ensemble averaged velocity field of the turbulent jet was simulated using the Reynolds Averaged Navier Stokes (RANS) equation. In principle this time averaged equation is time independent. Hence the steady state RANS equation for incompressible and isothermal flow reads

$$\rho\bar{\mathbf{u}}\cdot\nabla\overline{u_i} = -\frac{\partial\overline{p}}{\partial x_i}+\frac{\partial}{\partial x_i}[\overline{\tau}_{ij}+\tau_{ij}^R] \tag{2}$$

The over-bar represents an averaged quantity, the apostrophe the fluctuation from the average and the bold faced symbols represent vectors. Further, ρ is the fluid density, u is the fluid velocity, p is the pressure, x is the spatial coordinate, τ_{ij} are the stresses acting on the fluid and τ_{ij}^R are the Reynolds stresses. The Reynolds averaged continuity equation gives

$$\nabla\cdot\bar{\mathbf{u}} = 0 \tag{3}$$

The RANS equations with the Reynolds averaged continuity equation leave six degrees of freedom, the so-called Reynolds stresses.

$$\tau_{ij}^R = \rho\begin{pmatrix}\overline{u_1'^2} & \overline{u_1'u_2'} & \overline{u_1'u_3'}\\ \overline{u_2'u_1'} & \overline{u_2'^2} & \overline{u_2'u_3'}\\ \overline{u_3'u_1'} & \overline{u_3'u_2'} & \overline{u_3'^2}\end{pmatrix} \tag{4}$$

A method is needed to close the set of equations. Single-point closure models are relatively easy to implement and widely used in engineering. The Boussinesq hypothesis relates the Reynolds stresses to the mean strain rates via

$$-\overline{u_i'u_j'} = 2\nu_t\bar{S}_{ij}-\frac{2}{3}k\delta_{ij} \tag{5}$$

Here, δ_{ij} is the Kronecker delta, S_{ij} is the rate of strain tensor, k is the kinetic turbulent energy and ν_t is the eddy viscosity. Now the problem is shifted to finding the eddy viscosity at each point in the flow. In the k–ε model the eddy viscosity scales as follows:

$$\nu_t = C_\mu\frac{k^2}{\varepsilon} \tag{6}$$

In which ε is the turbulent energy dissipation and C_μ is a dimensionless constant. The transport equation for turbulent kinetic energy reads

$$\bar{\mathbf{u}}\cdot\nabla k = \left(\nu+\frac{\nu_t}{\sigma_k}\right)\Delta k+(\tau_{ij}^R/\rho)\bar{S}_{ij}-\varepsilon \tag{7}$$

And for turbulent energy dissipation

$$\bar{\mathbf{u}}\cdot\nabla\varepsilon = \left(\nu+\frac{\nu_t}{\sigma_\varepsilon}\right)\Delta\varepsilon+C_1\frac{\varepsilon}{k}(\tau_{ij}^R/\rho)\bar{S}_{ij}-C_2\frac{\varepsilon^2}{k} \tag{8}$$

In which ν is the kinematic viscosity of the liquid. In the transport equations for k and ε appear the following dimensionless parameters: σ_k, σ_ε, C_1 and C_2. The set of equations described here form a closed and solvable set of equations. The derivation of all equations can be found in any textbook (see e.g. Davidson, 2006, Chapter 4). In the k–ε models, there are only two parameters which characterize the turbulence. It is a simple model neglecting many details of the turbulent flow. Because the interest lies in the average energy dissipation inside a relatively large compartment there is no need to resolve the finer turbulence characteristics of the flow.

The k–ε model is the most frequently used engineering model of turbulence. It has proven to be reliable for simple shear flows but fails in complex configurations, high anisotropic turbulence and close to solid surfaces (Davidson, 2006, Chapter 4). There are many variations of the k–ε model with each having their own limitations which are well documented nowadays. The standard k–ε model and two of its more refined extensions (termed Realizable and RNG k–ε models) were experimentally validated for a scaled high pressure homogenizer using 2D Particle Image Velocimetry (PIV) (see Håkansson et al., 2011, 2012). The refined k–ε models give better estimates for the turbulent kinetic energy inside the narrow restriction. In the jet region the RNG model gives a slightly better prediction of the production of turbulent kinetic energy than its Realizable counterpart but is not well described by either model.

The RNG k–ε model was derived using a statistical technique called Re-Normalization Group theory. The RNG approach derived the transport equations for k and ε in a slightly different manner. The result is a different expression for the generation of turbulent kinetic energy from the mean velocity gradients. The transport equation for turbulent energy dissipation obtains the following additional parameters:

$$C_2 = C_2^*+\frac{C_\mu s^3(1-s/s_0)}{1+\beta s^3} \tag{9}$$

with

$$s = \sqrt{2S_{ij}S_{ij}}\frac{k}{\varepsilon} \tag{10}$$

Effectively this means that in areas of large strain ($s > s_0$) there is less dissipation of ε, a reduction of k and overall lower estimates of the eddy viscosity. Moreover, all constants are derived analytically with the RNG procedure, with the exception of β which needs to be fitted from experiment. The value of $\beta = 0.012$ has been found in the past and was taken as such. For the rest of the constants: $C_\mu = 0.0845$, $\sigma_k = 0.7194$, $\sigma_\varepsilon = 0.7194$, $C_1 = 1.42$, $C_2^* = 1.68$ and $s_0 = 4.38$. The RNG k–ε model is standard implemented in most CFD software packages with these default values.

4.1. Boundary conditions and numerical methods

The boundary conditions for the RANS equation at the homogenizer inlet was the velocity determined from the flow rate and at the outlet the gauge pressure was set to zero. At the walls the no-slip condition was applied. The velocity pressure coupling was solved numerically with the SIMPLE scheme and second order upwind discretization was used for all transport equations. The k–ε transport equations also need boundary conditions. At the inlet the flow is not turbulent; hence the kinetic turbulent energy and the turbulent energy dissipation were set to zero at the inlet. The turbulence modeling close to the walls needs some special attention and will be dealt with in the next section.

4.2. Modeling close to the wall and grid building

The remaining problem is the behavior of the k–ε model close to the solid boundaries. Near wall behavior of k–ε models is well known to give erroneous results (see e.g. Durbin and Pettersson-Reif, 2001, Chapter 6). Approaching the solid boundaries the viscous stresses outpace the inertial stresses. The fluid layer close to the wall where the viscous stresses cannot be neglected anymore is called the logarithmic layer. Therefore the k–ε equations are usually abandoned in the logarithmic layer. Instead, so-called wall functions for the production and dissipation of k are implemented. The boundary conditions for the k–ε model are then imposed on top of the logarithmic layer; however, in practice the boundary conditions are applied to the first grid point adjacent to the wall. Then, it is a necessary requirement for the first grid point to be located at the logarithmic layer. The first grid point must be located at a dimensionless normal distance to the wall of $y^+ \sim 15$ (ANSYS® Fluent, 2011, 14.0, help system, 4.13, ANSYS, Inc.). The distance normal to the wall is made dimensionless as follows:

$$y^+ = \frac{\sqrt{\tau_w/\rho}}{\nu}y \tag{11}$$

In which τ_w is the stress at the wall and y is the actual distance normal to the wall. Wall functions will give inaccurate results for a grid with $y^+ < 15$. In that situation a two layer zonal model will be more appropriate. In the two layer zonal model the momentum and turbulent kinetic energy equations are retained for both zones, since the turbulent kinetic energy is zero at the walls because of the no-slip condition. Only the ε transport equation is replaced by a mixing length transport equation in the zone adjacent to the wall, making this model also suitable for separating flows (recirculation) (Chen and Patel, 1988). In Fig. 4 two types of wall treatment are analyzed at the edges of the four compartments perpendicular to the flow.

The viscosity dominated region close to the walls should be relatively large because of the moderate Reynolds numbers. The Reynolds number in the channel and at the start of the jet, based on the channel height, is ~200. At these moderate Reynolds numbers no turbulence is generally expected for plane channel flow. Also at low Reynolds numbers the y^+ values remain fairly small for a coarse grid. In the high pressure homogenizer the most energy dissipation is expected to be in the center of the turbulent jet, which is observed with the two-layer zonal model, see Fig. 3. The standard wall function model over predicts the turbulent energy dissipation in close proximity of the boundary even at $y^+ = 14$. It appears that the two-layer zonal model gives the most physically reasonable results for the energy dissipation close to the walls.

From the discussion above the grid appears to be coarse for $y^+ < 15$, and then it follows that the two-layer zonal model is the preferred model. From a practical point of view a grid with a low resolution is preferred. Convergence of finer meshes was checked with respect to mass conservation and the quantity of interest: the average energy dissipation inside the compartments. Three meshes were constructed with a low, medium and high resolution. The three grids are compared in Table 2. A second-order upwind discretization scheme was used for the transport equations of momentum, turbulent kinetic energy (k) and turbulent dissipation rate (ε).

The difference between the mass flow rate at the in- and outlet was well below 1% for all meshes. The turbulent energy dissipation converged only for the meshes with a medium and high resolution. This difference in the integrated energy dissipation over the compartment volumes between the finer meshes was ~5%.

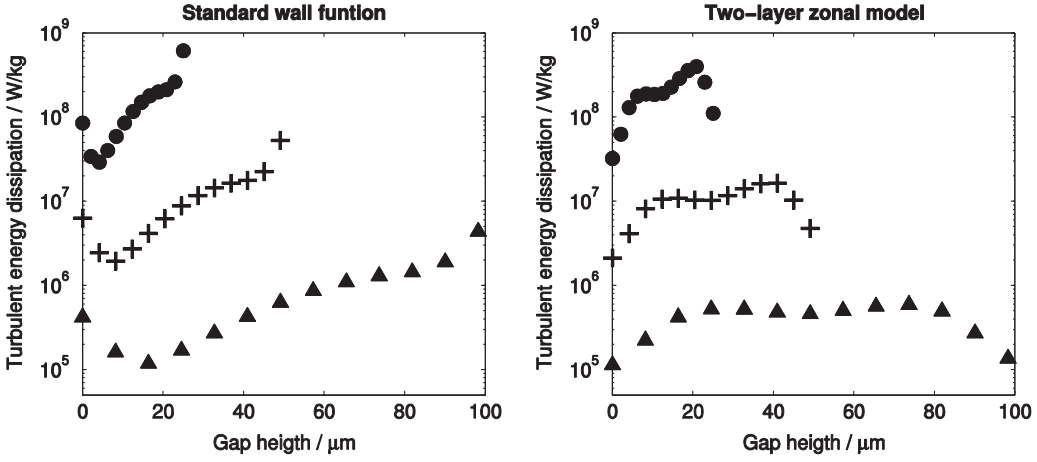

Fig. 4. The modeled turbulent energy dissipation at the edges of the compartments perpendicular to the flow; on the left the wall function model on the right the two-layer zonal model for $y+ = 14$; (•): boundary a, (+): boundary b and (▲): boundary c (see Fig. 3 for the boundaries).

For that reason the grid with the medium mesh resolution was selected to best fit the needs of this research.

4.3. CFD results

A Computational Fluid Dynamics (CFD) simulation was performed to estimate the local turbulent energy dissipation rates. The results of the CFD simulation are discussed here. The streamlines visualize the direction in which the emulsion travels through the homogenizer valve (Fig. 1). The emulsion flows around the impact head and leaves at the top. A vortex is formed in the corner of the passage head and the impact ring. The active part of the jet did not reach the vortex. No significant differences in the flow profiles were observed when changing the position of the valve to modify the pressure drop, results not shown.

The turbulent energy dissipation, which was correlated to droplet breakup, is displayed for the different parts of the homogenizer in a contour plot (Fig. 5). The largest energy dissipation was found directly after the narrow restriction. It was here where the droplet breakup was anticipated. The average and maximum of the turbulent energy dissipation are given in Table 3. The average energy dissipation per compartment was the highest directly after the gap and decreased exponentially with distance from the gap. The spread in the energy dissipation was also the highest in the first compartment (Table 3). In compartment 1 the average energy dissipation increases with increasing pressure drop. For the other three compartments, however, the average energy dissipation was slightly decreasing with pressure drop (Fig. 6). For now it is not certain whether this is caused by the CFD or this is actual physics.

5. Time scale analysis

In this section the time scales for several physical processes involving emulsification are discussed and compared to the residence times of the compartments which were defined in Section 3. The residence time (t_{res}) should be sufficiently long to deform the droplets. The droplets are deformed by eddies of approximately the same size. Therefore the eddy life time (t_{eddy}) should be of the same order as the deformation time or longer i.e. $t_{res} \geq t_{eddy} \geq t_{def}$. The residence time was compared to the time scales for droplet deformation and the eddy life time for a droplet of 10 μm in diameter (Table 3). Estimations for both times scales are given by Eqs. (12) and (13) (Walstra, 1993).

$$t_{def} \sim \frac{\eta_d}{5\rho_c \varepsilon^{2/3} d^{2/3}}, \tag{12}$$

where η_d is the dynamic viscosity of the dispersed phase, ρ_c is the continuous phase density, ε is the average energy dissipation (W kg^{-1}) and d is the droplet diameter. The eddy life time is based on an eddy with the same size as the mother droplet:

$$t_{eddy} \sim \frac{d^{2/3}}{\varepsilon^{1/3}} \tag{13}$$

Both time scales were calculated using the average energy dissipation in each compartment. The residence time in the four compartments was enough for eddies to appear and to disappear. The eddy life time in each compartment was sufficient to deform a droplet of 10 μm in diameter. It should be noted that a 10 μm

Table 2
Grid comparison.

Grid resolution	Number of cells along compartment border	Total number of cells	y^+
Low	12	24,995	14
Medium	35	37,806	5
High	50	54,366	3

Table 3
Results extracted from the CFD-simulation (800 bar pressure drop): the average ($\bar{\varepsilon}$) and maximum (ε_{max}) turbulent energy dissipation for the four compartments.

Compartment	$\bar{\varepsilon}$/W kg^{-1}	ε_{max}/W kg^{-1}
1	2.6E+10	3.3E+11
2	4.4E+07	2.9E+08
3	3.2E+06	1.1E+07
4	6.6E+05	1.6E+06

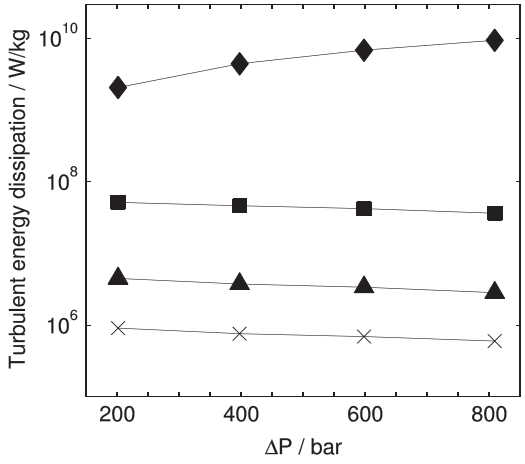

Fig. 6. The average energy dissipation as a function of pressure drop for the four compartments; (♦): compartment 1, (■): compartment 2, (▲): compartment 3 and (×): compartment 4.

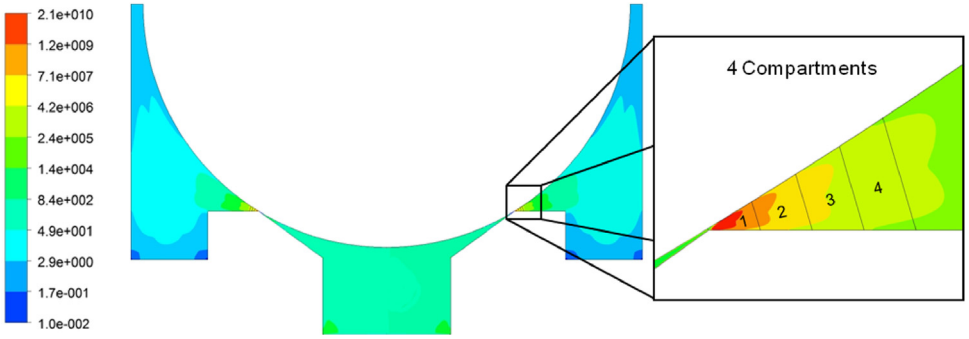

Fig. 5. The contours of the logarithm of the turbulent energy dissipation, the region directly after the narrow restriction is magnified and the four compartments can be seen.

droplet entered compartment 1 already in a deformed state, because the slit height is smaller than 1.6 μm for all experiments. This means that a large portion of the droplets passed through the slit as an elongated and/or flattened slug of oil.

Coalescence, on the other hand, is expected for droplets with surfactant depleted surfaces. Initially the droplet surfaces are completely covered with surfactant, because the surfactant was added in excess. In the compartments droplets are deformed and broken up and new interface is created allowing surfactant molecules to adsorb from the bulk. When the newly formed interface is completely covered the coalescence efficiency will drop to zero. Therefore, the surfactant adsorption time scale gives a good indication for where inside the homogenizer coalescence can be expected. The adsorption time scale for surfactant molecules in a turbulent flow, given by Walstra (1993), is presented here

$$t_{ads} \sim \frac{10\Gamma\eta_c^{1/2}}{dm_c\varepsilon^{1/2}} \tag{14}$$

In which Γ is the surface coverage, m_c is the critical micelle concentration, and the energy dissipation is given per unit of volume. The number of particle encounters in an isotropic turbulent flow (Walstra, 1993)

$$t_{enc} \sim \frac{d^{2/3}}{15\phi\varepsilon^{1/3}} \tag{15}$$

In Eq. (15), ϕ is the volume fraction of the dispersed phase. Because the average time a droplet encounters another droplet is lower than the adsorption time, see Table 4, coalescence is expected inside the compartments. This result was already experimentally confirmed by the oil transfer experiments of Taisne et al. (1996) where recoalescence was observed in the homogenizer valve.

6. Population balance modeling

The experimentally observed droplet size distribution in the homogenizer product stream is the result of droplet fragmentation and recoalescence. Therefore the following dynamic population balance was used including fragmentation and coalescence rates:

$$\begin{aligned}\frac{dn(v,t)}{dt} = &-g(v)n(v,t) + \int_v^\infty \beta(v,v')g(v')n(v',t)dv' \\ &- n(v,t)\int_0^\infty C(v,v')n(v',t)dv' \\ &+ \frac{1}{2}\int_0^v C(v-v',v')n(v-v',t)n(v',t)dv'\end{aligned} \tag{16}$$

Here v is the volume of the daughter droplet and v' of the mother droplet, n is the number density at time t, g is the breakage rate, C is the coalescence rate and β is the daughter droplet size distribution function. The population balance in Eq. (16) is an integro-differential equation and was solved by discretizing the size domain using the fixed pivot technique (Kumar and Ramkrishna, 1996). The total number of particles in size interval v_j to v_{j+1} per unit volume of emulsion, denoted N_j, is then given by

$$N_j(t) = \int_{v_j}^{v_{j+1}} n(v,t)dv \tag{17}$$

The flow rate through the homogenizer valve was constant; therefore the PBE (Eq. (16)) was integrated over the mean residence time spend in each compartment, see Fig. 3. The local conditions varied per compartment influencing the breakage and coalescence rates. Therefore the population balance was solved for each compartment. Eq. (16) needs to be supplied with initial conditions. The initial condition for the PBE of compartment 1 was the size distribution of the pre-emulsion. The size distribution obtained at the end of compartment 1 formed the initial condition for compartment 2 and so on for all compartments. The size distribution obtained in compartment 4 was assumed to be equal to the size distribution measured at the outlet of the homogenizer. The use of the PBE formulated in Eq. (16) requires sub-models for the breakup and coalescence rates, the daughter droplet size distribution and the number of daughter drops. The choices for the sub-models used will be outlined and discussed in this section.

6.1. The breakage rate model

Since turbulence prevails in the jet, a breakage function based on turbulent eddies was used. In reality there is a cascade of eddies, where large swirls are decomposed into smaller and smaller swirls. There are two droplet breakup mechanisms defined for turbulent flow. One mechanism is dominant when the mother droplets are of the same size as the eddies, this mechanism is referred to as turbulent inertial breakup. The other mechanism is prevalent when the mother droplets are smaller than the eddies, which is known as turbulent viscous breakup. An estimate for the smallest eddy size, which is still able to cause droplet breakup by pressure fluctuations, is the Kolmogorov length scale (l_e) (Vankova et al., 2007). The Kolmogorov length scale is given here

$$l_e = \eta_c^{3/4}\rho_c^{3/4}\varepsilon^{-1/4}, \tag{18}$$

where η_c and ρ_c are the viscosity and the density of the continuous phase respectively and ε is the average energy dissipation rate. It is important to distinguish between the two turbulent regimes since they each have a different effect on the droplet breakup and coalescence processes. Because the whole droplet size distribution is considered there will be droplets smaller than the Kolmogorov length scale, this can be seen by comparing the droplet size measurements in Fig. 2 with the calculated Kolmogorov length scales collected in Table 5. The question now arises whether these small droplets are likely to breakup inside eddies or not. The maximum stable droplet size in the turbulent viscous regime, denoted by d_{TV}, can be estimated by comparing the Laplace pressure ($=4\sigma/d$) of the droplet with the viscous stress inside the eddy

$$d_{TV} \sim \sigma\eta_c^{-1/2}\rho_c^{-1/2}\varepsilon^{-1/2} \tag{19}$$

It appears that d_{TV} is larger than the Kolmogorov length scale when the average and maximum energy dissipation are considered in each compartment. This means that the small portion of droplets which are located inside eddies will not fragment because their Laplace pressure is too high. The effects of the turbulent viscous regime on droplet breakup become apparent at energy dissipation rates of $>10^{11}\,\mathrm{W\,kg^{-1}}$ for the current emulsion formulation. Another option is to increase the viscosity of the continuous phase to >3 times that of water (Vankova et al., 2007). Therefore only the turbulent inertial regime is considered for droplet breakup. The rate of droplet breakup in the turbulent inertial regime is given in Eq. (20) (Coulaloglou and Tavlarides,

Table 4
The residence time (t_{res}) compared to the time scales for droplet deformation (t_{def}), eddy life time (t_{eddy}), surfactant adsorption time (t_{ads}) and droplet-droplet encounter time (t_{enc}) in the four compartments at 800 bar pressure drop.

Compartment	t_{res}/s	t_{def}/s	t_{eddy}/s	t_{ads}/s	t_{enc}/s
1	2.4E−06	2.5E−09	1.6E−07	1.1E−08	3.0E−09
2	7.1E−06	1.7E−07	1.3E−06	1.7E−07	4.8E−08
3	1.2E−05	9.9E−07	3.1E−06	6.1E−07	1.7E−07
4	1.7E−05	2.8E−06	5.3E−06	1.3E−06	3.7E−07

Table 5
the Kolmogorov length scale (l_e) and the maximum droplet size according to Eq. (19). Calculated with the average energy dissipation from Table 2.

Compartment	l_e/μm	d_{TV}/μm
1	0.12	0.15
2	0.50	2.48
3	0.94	8.84
4	1.38	19.25

1977):

$$g(v) = K_1 \frac{v^{-2/9}\bar{\varepsilon}^{1/3}}{(1+\phi)} \exp\left(-\frac{K_2\sigma(1+\phi)^2}{\rho_d v^{5/9}\bar{\varepsilon}^{2/3}}\right), \tag{20}$$

where K_1 and K_2 are adjustable dimensionless parameters, σ is the interfacial tension and ρ_d is dispersed phase density. Eq. (20) is a combination of the breakage frequency and the breakage probability (the exponential term). The breakage frequency is increasing for smaller droplets. The breakage probability is approximately equal to one for all droplet sizes larger than the maximum stable droplet size. The factor $1/(1+\phi)$ accounts for damping of turbulence by the dispersed phase (Coulaloglou and Tavlarides, 1977).

6.2. The daughter droplet size distribution function

From single droplet experiments a lot can be learned about the breakup behavior of droplets with respect to the number of fragments and the sizes of the daughter droplets. Andersson and Andersson (2006) observed single droplet breakup with a high speed camera and concluded that equal sized breakup is the most probable. In this work the daughter droplet size distribution function was assumed to be a uniform probability function, meaning that the droplets obtained after a breakage event have the same size. The uniform daughter droplet size distribution function for multiple breakup was derived by (Hill and Ng, 1996)

$$\beta(v,v') = p(p-1)\left(1-\frac{v}{v'}\right)^{p-2}, \tag{21}$$

where p is the number of daughter droplets. In turbulent flows viscous droplets were shown to stretch to long threads, up to 20 times the initial droplet diameter (Andersson and Andersson, 2006). The thread diameter then becomes $\sim 0.18d$, based on the conservation of volume. The breakup of liquid viscous threads is caused by small disturbances present on the interface which grow and disintegrate the liquid cylinder because the interfacial tension tends to minimize the interfacial area between two phases. The fragment size depends on the viscosity ratio for liquid thread breakup. For the current formulation, the daughter droplet size becomes 3.2 times the thread diameter, using the analysis of Janssen and Meijer (1995), which results into five daughter droplets.

6.3. The coalescence rate model

The coalescence rate is modeled as the product of the collision frequency $h(v, v')$ and the coalescence efficiency $\Lambda(v, v')$, since not all collisions lead to coalescence, especially not when a surface active component is present. The coalescence rate reads

$$C(v,v') = h(v,v')\Lambda(v,v') \tag{22}$$

Coulaloglou and Tavlarides (1977) proposed to use the kinetic theory of gasses to derive the turbulent random motion-induced collision frequency between droplets of size v and v', which is given here

$$h(v,v') = \frac{K_3\varepsilon^{1/3}}{(1+\phi)}(v^{2/3}+v'^{2/3})(v^{2/9}+v'^{2/9})^{1/2} \tag{23}$$

In which K_3 is a dimensionless adjustable parameter and the factor $1/(1+\phi)$ accounts, likewise, for the damping of turbulence by the dispersed phase. Eq. (23) is often encountered in the literature to describe the collision frequency. Although more comprehensive models exist, for example which take the eddy size into account, the goal is not to make the modeling exercise too elaborate. More advanced models can be found in a recent review paper published by Liao and Lucas (2010).

The coalescence efficiency is based on the film drainage model, which is also one of the most frequently applied models for coalescence efficiency (Liao and Lucas, 2010). The efficiency is one when the contact time between droplets is greater than the film drainage time. The coalescence efficiency then reads

$$\Lambda(v,v') = \exp\left(-\frac{t_{drain}}{t_{contact}}\right). \tag{24}$$

The drainage time is the time required for the liquid film to drain from between the droplets. For deformable particles with immobile interfaces, Coulaloglou and Tavlarides (1977) estimated the drainage time as

$$t_{drain} \sim \frac{\eta_c\rho_c\varepsilon^{2/3}(v+v')^{2/9}}{\sigma^2}\left(\frac{1}{h^2}-\frac{1}{h_0^2}\right)\left(\frac{v^{1/3}v'^{1/3}}{v^{1/3}+v'^{1/3}}\right)^4 \tag{25}$$

In which h and h_0 are the critical and initial film thickness; they are replaced by a fit parameter. The approximation of immobility of the film surface is applicable to systems with a high viscosity ratio and/or surfactant dissolved in the continuous phase (Chesters, 1991). Coulaloglou and Tavlarides (1977) estimated the contact time by a dimensional analysis from Levich (1962)

$$t_{contact} \sim \frac{(v+v')^{2/9}}{\varepsilon^{1/3}} \tag{26}$$

The coalescence rate becomes

$$C(v,v') = K_3\frac{\varepsilon^{1/3}}{(1+\phi)}(v^{2/3}+v'^{2/3})(v^{2/9}+v'^{2/9}) \times \exp\left(-K_4\frac{\eta_c\rho_c\varepsilon}{\sigma^2(1+\phi)^3}\left(\frac{v^{1/3}v'^{1/3}}{v^{1/3}+v'^{1/3}}\right)^4\right). \tag{27}$$

6.4. Parameter optimization

The free parameters (K_1 up to K_4) can be obtained by comparing the model with the experimental results via a least squares optimization. Parameters K_{1-3} were expected to be of the order unity because of the derivation of the model equations. Parameter K_4, however, was anticipated to be a large number because the term with the film thickness (see Eq. (25)) was clustered together with the empirical constant, K_4. The parameters K_1 up to K_4 of the breakage and coalescence rates were found by minimizing the following objective function:

$$\Psi = \frac{\sum_j^M (n_{\exp}^{[j]} - \phi_j)^2}{\sum_j^M (n_{\exp}^{[j]})^2}, \tag{28}$$

here M is the number of discrete size classes, n_{exp} is the measured volume fraction of droplets in size class j and ϕ_j is the volume fraction of droplets in size class j. The volume fraction of droplets in size class j was calculated from the discreet average number of droplets in size class j, by using

$$\phi_j = \frac{N_j v_j}{\phi} \tag{29}$$

The optimization problem appeared to be non-convex, for that reason the Genetic Algorithm (Matlab (MATLAB and Global Optimization Toolbox R (2013)), a global non-linear optimization algorithm, was used to find the adjustable parameter values corresponding to the lowest objective function value. Two datasets were used for the optimization of the parameters. The datasets were the size distributions obtained from the experiments at 200 and 800 bar after one pass through the homogenizer. The remaining datasets were used to test the performance of the model with the fitted parameters. In all cases the objective function in Eq. (28) was used to judge the quality of the model predictions versus the experimental observations.

7. Results and discussion

7.1. Prediction of droplet size distributions for single pass processing

The main objective of this work was to predict the droplet size distributions subject to various hydrodynamic conditions in a high pressure homogenizer. This means that one set of parameters should be able to describe the change in the droplet size distribution for a range of operating conditions. The predictions of the compartment model were compared to the measured droplet size distributions in Fig. 7 for four different pressures and one pass through the homogenizer valve. Considerable improvements were observed when comparing the model predictions of the first pass with the results of the work of Raikar et al. (2009, 2010, 2011) or Becker et al. (2013). Note that Maindarkar et al. (2012) obtained reasonable objective function values for the different pressures, but the fit parameters were recalculated for each pressure drop and two extra fit parameters were used.

The droplet size development through the compartments is shown in Fig. 8. In compartment 1 the largest size reduction occurred. In compartments 2, 3 and 4 the average droplet size appeared to increase. It has been argued that in the latter part of the active turbulent jet the effect of coalescence might be more important than the effect of breakage (Håkansson et al., 2009). It was assumed that the droplet size distribution leaving compartment 4 is equal to droplet size distribution leaving the homogenizer. Note that the droplet size distribution leaving the homogenizer was measured. Indeed, from the simulation results (Fig. 8) it can be observed that the average droplet size in compartment 4 is hardly affected by breakage and coalescence phenomena. It should be pointed out that the droplet sizes in between the compartments could not be verified experimentally. Only the Sauter mean diameter at the outlet of compartment four can be compared to experimental means, see Fig. 9. Looking at the average droplet sizes in Fig. 9, it appears that the model underestimated for 200 and 400 bar and overestimated for 600 and 800 bar.

7.2. Prediction of droplet size distributions for multi-pass processing

Experiments have shown to yield mono-modal droplet size distributions after multiple passes through the high pressure

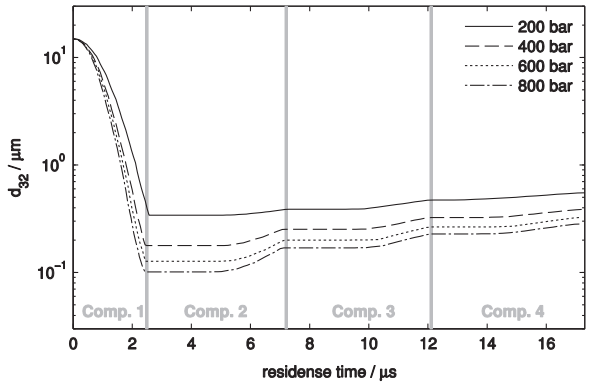

Fig. 8. Sauter mean diameter through the compartments of the high pressure homogenizer at various pressures.

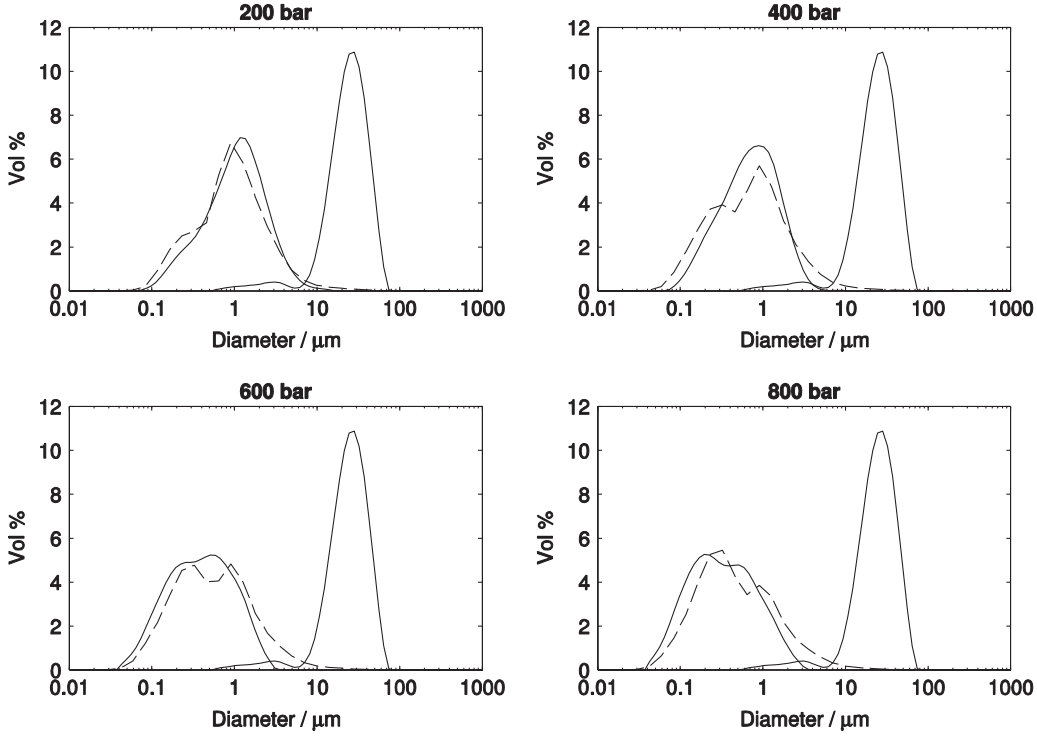

Fig. 7. The simulated (dashed black line), measured inlet (gray line) and outlet (black line) droplet size distributions: (a) for 200 bar with Ψ=0.0503, (b) for 400 bar with Ψ=0.0867, (c) for 600 bar with Ψ=0.0243 and (d) for 800 bar with Ψ=0.0198.

homogenizer. In Fig. 10, the droplet size distributions after one, two and three passes for the four different pressures are displayed. In this simulation still the same set of parameters was used as for the single pass experiments in Figs. 7–9. The width of the distribution became narrower when the emulsion was passed several times through the homogenizer (Fig. 10). This was also experimentally observed for different types of homogenizers by Becker et al. (2013) and Maindarkar et al. (2013). The population balance model rendered mono-modal droplet size distributions after two passes, but no significant change was observed after the third pass.

The model performance was quantified by the objective function value given in Eq. (28). The performances of three models are given in Table 7. The four compartment model was compared to a model comprising one compartment and a model with two compartments. In the second column the objective function was summed over the different operating pressures for a single pass through the homogenizer. Increasing the number of compartments improved the model predictions. The model with two compartments improved the objective function value by 33% for one pass through the homogenizer. Only considering multiple passes the two-compartment model performed worse than the one-compartment model. Regarding all experiments, the four-compartment model performed 23% better than the one-compartment model.

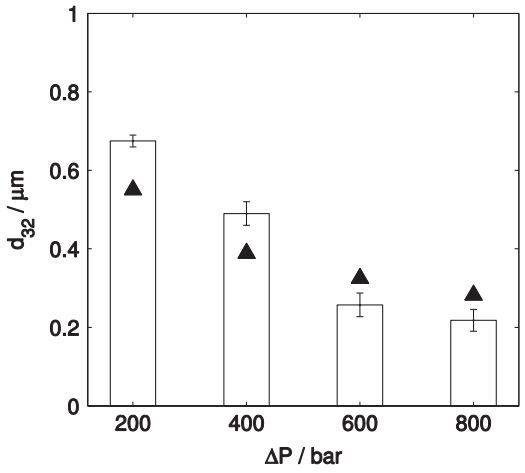

Fig. 9. The measured Sauter mean diameters for four different pressures after a single pass (bar plot) including an error bar versus the simulated droplet sizes from the four compartment model (triangles).

7.3. Discussion on the fit parameters

The breakage and coalescence functions derived by Coulaloglou and Tavlarides (1977), i.e. Eqs. (20) and (27), are often used to model size distributions of bubbles or droplets for various types of equipment.

The breakage and coalescence equations contain free parameters so that the model is adjustable to many experimental observations. It is interesting to compare the parameters found by other authors who used the same model for breakage and coalescence, see Table 6. There are a lot of notable differences between the different types of mixers and even for the same type of mixer (high pressure homogenizer) the parameter values vary several orders of magnitude. It is, however, not possible to quantitatively compare the parameter values, because the end result also depends on the choice of binary or multiple breakup, number of fragments and daughter droplet size distribution function and to a minor extent on the discretization algorithm and number of size classes. Therefore only the breakage rates as a function of the mother droplet size are compared in Fig. 11.

The model from Raikar et al. (2010), for example, also included a droplet breakage rate for the turbulent viscous regime and excluded the coalescence rate. In the breakage rate for turbulent inertial breakup the damping of turbulent energy dissipation in the breakup frequency was neglected, nonetheless parameter K_1 is

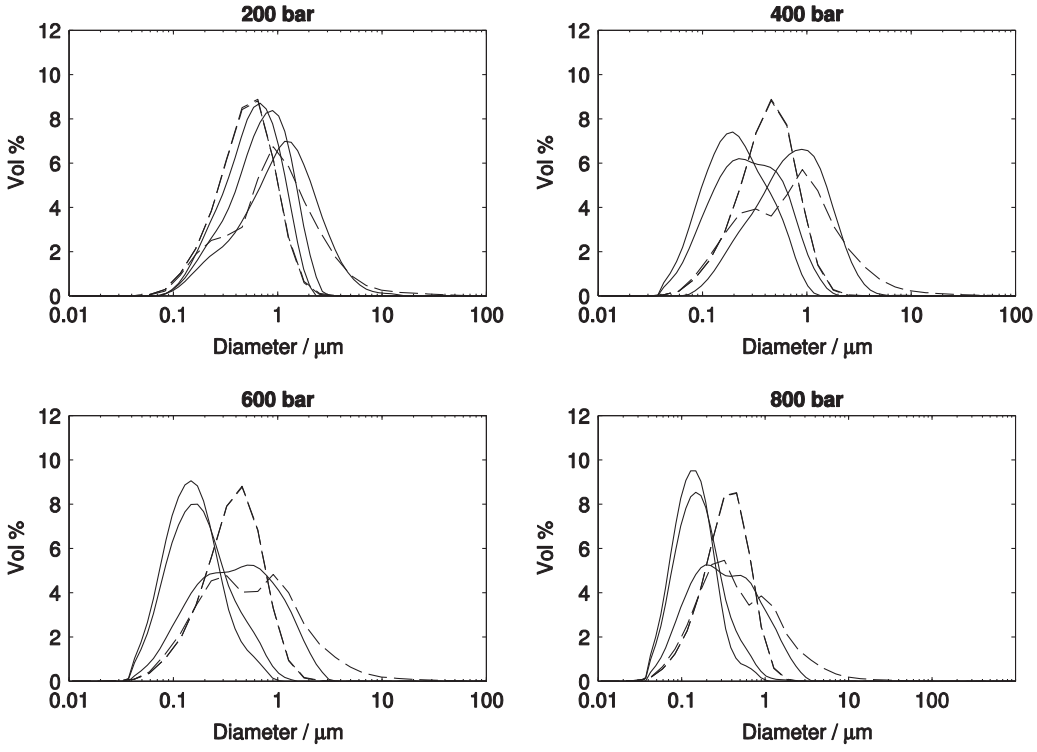

Fig. 10. The measured (continuous lines) and simulated (dashed lines) droplet size distributions for 3 passes through the homogenizer; the size distribution curves move to the left after each pass i.e. the droplets become smaller. The simulated size distributions for passes 2 and 3 overlap.

Table 6
The obtained values for the fit parameters of the four compartment model in comparison with the work of other authors.

	High pressure homogenizers				Stirred vessel	Static mixer	Single droplet experiment
	This work: Four compartment model	This work: Single compartment model	Raikar et al. (2011)	Vankova et al. (2007)	Coulaloglou and Tavlarides (1977)	Azizi and Al Taweel. (2011)	Maaß and Kraume (2012)
K_1	1.47	1.81	2.62×10^{-8}	0.033	0.40	0.86	0.91
K_2	1.14	0.53	0.175	3.6	0.08	4.1	0.39
K_3	0.087	1.99	–	–	2.8	0.04	–
K_4/m^{-2}	20,420	101	–	–	1.83×10^5	1×10^{10}	–

Table 7
The summed objective function (Ψ).

Model	Single pass experiments	All experiments
1 Compartment	0.60	4.8
2 Compartments	0.40	5.1
4 Compartments	0.21	3.7

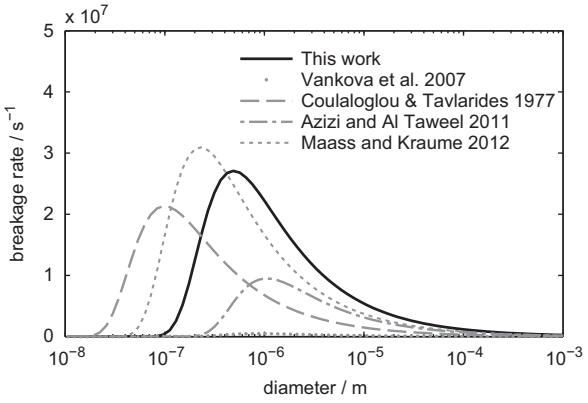

Fig. 11. The breakage rates as a function of the droplet size from several authors; all breakage rate functions are based on the original Eq. (20).

extremely small in comparison with all others. As a consequence the total breakage rate is extremely small under set conditions and cannot be shown in Fig. 11. Vankova et al. (2007) used a slightly adjusted model for their narrow gap homogenizer. Likewise, the damping terms and coalescence rate are neglected but a factor including the square root of the density ratio was added. The static mixer of Azizi and Al Taweel (2011) was divided up into several compartments as well and they were able to find one set of parameters describing the full range of their experimental conditions. The parameter values from the original paper of Coulaloglou and Tavlarides (1977) also did not match any other set of parameters. The reason that the parameter values deviated was that the energy dissipation rate near the impeller was estimated 70 times the average energy dissipation.

Droplets will experience only the hydrodynamic forces in their proximity and not the average inside a vessel or valve. In the experiments of Maaß and Kraume (2012) single droplet breakup events were monitored and the breakage function (Eq. (20)) was fitted to their data. This approach offers most likely more general parameter values. Because the breakage rate function was fitted to single droplet breakup events, instead of fitting the PBE to the droplet size distribution obtained after a myriad of breakup events. For that reason the parameters of Maaß and Kraume (2012) were tested in the population balance approach with the four compartments. The coalescence parameters K_3 and K_4 were retained from the earlier fit. The average droplet sizes were matching relatively well with objective function values of $\Sigma\Psi=0.78$ for the first pass experiments and $\Sigma\Psi=3.8$ for all experiments. But closer inspection of the size distribution showed bimodality and a wider spread of the droplet sizes.

8. Conclusions

The approach presented in this paper offered good predictions of the complete droplet size distribution under various hydrodynamic conditions without excessive computational times. A CFD simulation was executed first and four compartments were defined directly after the narrow restriction. The average energy dissipation was calculated for each compartment. The energy dissipation rates were included in the PBE model. The free parameters in the model were adjusted to obtain a good fit of the experimental data. The extensibility of the model was tested at various pressures for one pass and multiple passes through the high pressure homogenizer at constant pressure. All in all the parameter values obtained in this work predicted the size distribution well within the experimental range of the homogenizing apparatus but are expected to remain equipment dependent.

In order to have predictive control over the droplet size distribution in a homogenizing apparatus the hydrodynamic features are of importance. In most types of equipment there is no homogeneous energy dissipation. There are regions where the energy intensity is high, for example close to a stirrer or inside a jet. Then it is recommended to divide up the device in so-called compartments in order to minimize the inhomogeneity. It has been demonstrated here that the use of four compartments with each having its own average turbulent energy dissipation improved the model predictions by 65% compared to the single compartment model. Increasing the number of compartments will evidently lead to better results but a penalty must be paid because the optimization time increases. The compartment approach may provide an alternative to the direct coupling of population balances with Computational Fluid Dynamics. The compartment approach is computationally less expensive than direct coupling; moreover, direct coupling is physically questionable for geometries where the droplet size is equal or bigger than the confined geometry.

Nomenclature

Abbreviations

CFD	Computational Fluid Dynamics
PBE	population balance equations
PIV	Particle Image Velocimetry
QMOM	Quadrature Method of Moments
RANS	Reynolds Averaged Navier Stokes
RNG	Re-Normalization Group

Latin letters

$C(v, v')$	coalescence rate/m^3 s^{-1}
d	droplet diameter/m
$d32$	Sauter mean diameter/m
d_{v99}	cumulative diameter, $P(d \leq d_{v99})=0.99$/m
$g(v)$	breakage rate/s^{-1}
$h(v, v')$	collision frequency/m^3 s^{-1}
k	turbulent kinetic energy/J kg^{-1}
K_{1-4}	fit parameters
l_e	Kolmogorov length scale/m
M	number of discreet size classes
m_c	critical micelle concentration/mol m^{-3}
$n_v(v,t)$	droplet volume fraction of size v at time t
N	number of size classes
p	number of daughter droplets
r	radial coordinate/m
r_0	point where jet becomes self-similar/m
S	strain rate/s^{-1}
t	time/s
u	fluid velocity/m s^{-1}
u'	fluid velocity fluctuation/m s^{-1}
$\bar{u}_0$	jet center line velocity/m s^{-1}
U_0	jet speed where the jet becomes self-similar/m s^{-1}
v	daughter droplet volume/m^3
v'	mother droplet volume/m^3
V	compartment volume/m^3
x_i	spatial coordinates/m
z	axial coordinate/m

Greek letters

α	entrainment coefficient
$\beta(v, v')$	daughter droplet size distribution function
Γ	surface coverage/mol m^{-2}
δ_0	jet height where the jet becomes self-similar/m
δ_{ij}	Kronecker delta
ε	turbulent energy dissipation rate/W kg^{-1}
η	dynamic viscosity/Pa s
ν	kinematic viscosity/m^2 s
ν_t	eddy viscosity/m^2 s
ρ	density/kg m^{-3}
τ_{ij}	stresses/Pa
τ_{ij}^R	Reynolds stresses/Pa
ϕ	dispersed phase volume fraction
σ	interfacial tension/N m^{-1}
Ψ	objective function value

Subscripts

c	continuous phase
d	dispersed phase
def	deformation
j	index for a size class
res	residence
TV	turbulent viscous
v	volume based

Acknowledgment

The authors wish to thank Unilever Research and Development in Vlaardingen, The Netherlands for financial support.

References

ANSYS® Fluent, 14.0, Help system, 2011. Ch. 4.13: Near-Wall Treatments for Wall-Bounded Turbulent flows, ANSYS, Inc.
Agterof, W., Vaessen, G., Haagh, G., Klahn, J., Janssen, J., 2003. Prediction of emulsion particle sizes using a computational fluid dynamics approach. Colloids Surf. B: Biointerfaces 31 (1–4), 141–148.
Alexopoulos, A., Maggioris, D., Kiparissides., C., 2002. CFD analysis of turbulence non-homogeneity in mixing vessels a two-compartment model. Chem. Eng. Sci. 57 (10), 1735–1752.
Almeida-Rivera, C., Bongers, P., 2010. Modelling and experimental validation of emulsification processes in continuous rotor–stator units. Comput. Chem. Eng. 34 (5), 592–597.
Alopaeus, V., Koskinen, J., Keskinen, K., 1999. Simulation of the population balances for liquid–liquid systems in a nonideal stirred tank. Part 1 description and qualitative validation of the model. Chem. Eng. Sci. 54 (24), 5887–5899.
Andersson, R., Andersson, B., 2006. On the breakup of fluid particles in turbulent flows. AIChE J. 52 (6), 2020–2030.
Azizi, F., Al Taweel, A.M., 2011. Turbulently flowing liquid–liquid dispersions. Part I: Drop breakage and coalescence. Chem. Eng. J. 166, 715–725.
Becker, P., Dubbelboer, A., Sheibat-Othman, N., 2013. A coupled population balance cfd framework in openfoam for a high pressure homogenizer. Récents Prog. Génie Procédés 104, 2981–2988.
Blonski, S., Korczyk, P., Kowalewski, T., 2007. Analysis of turbulence in a micro-channel emulsifier. Int. J. Ther. Sci. 46 (11), 1126–1141.
Casoli, P., Vacca, A., Berta, G., 2010. A numerical procedure for predicting the performance of high pressure homogenizing valves. Simul. Model. Pract. Theory 18 (2), 125–138.
Chen, H.C., Patel, V.C., 1988. Near-wall turbulence models for complex flows including separation. AIAA J. 26 (6), 641–648.
Chesters, A.K., 1991. The modelling of coalescence processes in fluid-liquid dispersions: a review of current understanding. Trans. IChemE 69 (Part A), 259–270.
Coulaloglou, C., Tavlarides, L., 1977. Description of interaction processes in agitated liquid–liquid dispersions. Chem. Eng. Sci. 32 (11), 1289–1297.
Davidson, P.A., 2006. Turbulence: An Introduction for Scientists and Engineers, third ed. Oxford University Press, Great Claredon Street, Oxford (Chapter 4).
Drumm, C., Attarakih, M., Bart, H.J., 2009. Coupling of cfd with dpbm for an rdc extractor. Chem. Eng. Sci. 64 (4), 721–732.
Dubbelboer, A., Janssen, J., Hoogland, H., Mudaliar, A., Zondervan, E., Bongers, P., Meuldijk., J., 2013. A modeling approach for dispersive mixing of oil in water emulsions. Comput. Aided Chem. Eng. 32, 841–846.
Durbin, P.A., Pettersson-Reif, B.A., 2001. Statistical Theory and Modeling for Turbulent Flows (Chapter 6). First ed. John Wiley And Sons Ltd..
Fathi Roudsari, S., Turcotte, G., Dhib, R., Ein-Mozaffari., F., 2012. Cfd modeling of the mixing of water in oil emulsions. Comput. Chem. Eng. 45, 124–136.
Floury, J., Bellettre, J., Legrand, J., Desrumaux, A., 2004a. Analysis of a new type of high pressure homogeniser. A study of the flow pattern. Chem. Eng. Sci. 59 (4), 843–853.
Floury, J., Legrand, J., Desrumaux, A., 2004b. Analysis of a new type of high pressure homogeniser. Part b. Study of droplet break-up and recoalescence phenomena. Chem. Eng. Sci. 59 (6), 1285–1294.
Håkansson, A., Trägårdh, C., Bergenståhl, B., 2009. Studying the effects of adsorption, recoalescence and fragmentation in a high pressure homogenizer using a dynamic simulation model. Food Hydrocoll. 23 (4), 1177–1183.
Håkansson, A., Fuchs, L., Innings, F., Revstedt, J., Trägårdh, C., Bergenståhl, B., 2011. High resolution experimental measurement of turbulent flow field in a high pressure homogenizer model and its implications on turbulent drop fragmentation. Chem. Eng. Sci. 66 (8), 1790–1801.
Håkansson, A., Fuchs, L., Innings, F., Revstedt, J., Trägårdh, C., Bergenståhl, B., 2012. Experimental validation of k–ε rans-cfd on a highpressure homogenizer valve. Chem. Eng. Sci. 71, 264–273.
Håkansson, A., Innings, F., Trägårdh, C., Bergenståhl, B., 2013a. A high pressure homogenization emulsification model-improved emulsifier transport and hydrodynamic coupling. Chem. Eng. Sci. 91, 44–53.
Håkansson, A., Fuchs, L., Innings, F., Revstedt, J., Trägårdh, C., Bergenståhl, B., 2013b. Velocity measurements of turbulent two-phase flow in a high-pressure homogenizer model. Chem. Eng. Commun. 200 (1), 93–114.
Hill, P., Ng, K., 1996. Statistics of multiple particle breakage. AIChE J. 42 (6), 1600–1611.
Innings, F., Trägårdh, C., 2007. Analysis of the flow field in a high pressure homogenizer. Exp. Ther. Fluid Sci. 32 (2), 345–354.
Janssen, J.M.H., Meijer, H.E.H., 1995. Dynamics of liquid–liquid mixing: a 2-zone model. Polym. Eng. Sci. 35 (22), 1766–1780.
John, V., Angelov, I., Öncül, A., Thévenin, D., 2007. Techniques for the reconstruction of a distribution from a finite number of its moments. Chem. Eng. Sci. 62 (11), 2890–2904.
Karbstein, H., Schubert, H., 1995. Developments in the continuous mechanical production of oil-in-water macro-emulsions. Chem. Eng. Process.: Process Intensif. 34 (3), 205–211.
Kumar, S., Ramkrishna, D., 1996. On the solution of population balance equations by discretization – I. A fixed pivot technique. Chem. Eng. Sci. 51 (8), 1311–1332.
Levich, V.G., 1962. Physicochemical Hydrodynamics. Prentice-Hall, Englewood Cliffs.
Liao, Y., Lucas, D., 2009. A Literature review of theoretical models for drop and bubble breakup in turbulent dispersions. Chem. Eng. Sci. 64 (15), 3389–3406.
Liao, Y., Lucas, D., 2010. A Literature review on mechanisms and models for the coalescence process of fluid particles. Chem. Eng. Sci. 65 (10), 2851–2864.

Luckham, Paul F., Ukeje, Michael A., 1999. Effect of particle size distribution on the rheology of dispersed systems. J. Colloid Interface Sci. 220, 347–356.
Luo, H., Svendsen, H.F., 1996. Theoretical model for drop and bubble breakup in turbulent dispersions. AIChE J. 42 (5), 1225–1233.
MATLAB and Global Optimization Toolbox R, 2013. The MathWorks, Inc., Natick, Massachusetts, United States.
Maaß, S., Kraume, M., 2012. Determination of breakage rates using single drop experiments. Chem. Eng. Sci. 70, 146–164.
Maindarkar, S., Raikar, N., Bongers, P., Henson, M., 2012. Incorporating emulsion drop coalescence into population balance equation models of high pressure homogenization. Colloids Surf. A: Physicochem. Eng. Asp. 396, 63–73.
Maindarkar, S., Bongers, P., Henson, M., 2013. Predicting the effects of surfactant coverage on drop size distributions of homogenized emulsions. Chem. Eng. Sci. 89, 102–114.
McClements, D.J., Chanamai, R., 2002. Physicochemical properties of monodisperse oil-in-water emulsions. J. Dispers. Sci. Technol. 23 (1–3), 125–134.
McClements, David Julian, Yan, Li, 2010. Structured emulsion-based delivery systems: controlling the digestion and release of lipophilic food components. Adv. Colloid Interface Sci. 159, 213–228.
Phipps, L., 1975. The fragmentation of oil drops in emulsions by a high pressure homogenizer. J. Phys. D: Appl. Phys. 8 (4), 448–462.
Raikar, N., Bhatia, S., Malone, M., Henson, M., 2009. Experimental studies and population balance equation models for breakage prediction of emulsion drop size distributions. Chem. Eng. Sci. 64 (10), 2433–2447.
Raikar, N., Bhatia, S., Malone, M., McClements, D., Almeida-Rivera, C., Bongers, P., Henson, M., 2010. Prediction of emulsion drop size distributions with population balance equation models of multiple drop breakage. Colloids Surf. A: Physicochem. Eng. Asp. 361 (1–3), 96–108.
Raikar, N., Bhatia, S., Malone, M., McClements, D., Henson, M., 2011. Predicting the effect of the homogenization pressure on emulsion drop size distributions. Ind. Eng. Chem. Res. 50 (10), 6089–6100.
Scheffold, F., Cardinaux, F., Mason, T.G., 2013. Linear and nonlinear rheology of dense emulsions across the glass and the jamming regimes. J. Phys.: Condens. Matter 25, 502101 (5 pp.).
Schuchmann, H., Schubert, H., 2001. Emulsification in high-pressure homogenizers. Chem. Eng. Technol. 24 (10), 151–157.
Schultz, S., Wagner, G., Urban, K., Ulrich, J., 2004. High-pressure homogenization as a process for emulsion formation. Chem. Eng. Technol. 27 (4), 361–368.
Silva, L., Damian, R., Lage, P., 2008. Implementation and analysis of numerical solution of the population balance equation in cfd packages. Comput. Chem. Eng. 32 (12), 2933–2945.
de Souza, L., Janiga, G., John, V., Thévenin, D., 2010. Reconstruction of a distribution from a finite number of moments with an adaptive splinebased algorithm. Chem. Eng. Sci. 65 (9), 2741–2750.
Steiner, H., Teppner, R., Brenn, G., Vankova, N., Tcholakova, S., Denkov, N., 2006. Numerical simulation and experimental study of emulsification in a narrow-gap homogenizer. Chem. Eng. Sci. 61 (17), 5841–5855.
Taisne, Laurent, Walstra, Pieter, Cabane, Bernard, 1996. Transfer of oil between emulsion droplets. J. Colloid Interface Sci. 184, 378–390.
Vankova, N., Tcholakova, S., Denkov, N., Ivanov, I., Vulchev, V., Danner, T., 2007. Emulsification in turbulent flow. 1. mean and maximum drop diameters in inertial and viscous regimes. J. Colloid Interface Sci. 312 (2), 363–380.
Walstra, P., 1993. Principles of emulsion formation. Chem. Eng. Sci. 48 (2), 333–349.